

Article

# Fabrication and Actuation Performance of Selective Laser Melting Additive-Manufactured Active Shape-Memory Alloy Honeycomb Arrays

Yuesheng Xu, Lei Qiu \* and Shenfang Yuan \*

Research Center of Structural Health Monitoring and Prognosis, State Key Laboratory of Mechanics and Control of Mechanical Structures, College of Aerospace Engineering, Nanjing University of Aeronautics and Astronautics, Nanjing, 29 Yudao Street, Nanjing 210016, China

\* Correspondence: lei.qiu@nuaa.edu.cn (L.Q.); ysf@nuaa.edu.cn (S.Y.)

**Abstract:** Shape-memory alloy (SMA) honeycomb arrays have drawn worldwide attention for their potential active applications in smart morphing wings. However, the manufacturing of complex active SMA honeycomb arrays via conventional processes is a difficult task, and the actuation performance of the honeycomb arrays has not yet been well-investigated. In this work, the active SMA honeycomb arrays were fabricated by selective laser melting (SLM) additive manufacturing, and their actuation performance was investigated. The results show that the SLM-fabricated active SMA honeycomb arrays can generate obvious actuation performance during the transformation and exhibit a higher maximum actuation stress of 2.53 MPa at a  $R/t$  ratio of 4 and a tensile pre-strain of 35%. This research will contribute to the design and further improvement of active SMA honeycomb arrays based on SLM additive manufacturing, promoting the engineering applications for smart morphing wings.

**Keywords:** smart morphing wings; additive manufacturing; shape-memory alloy; honeycomb arrays; actuation performance



**Citation:** Xu, Y.; Qiu, L.; Yuan, S. Fabrication and Actuation Performance of Selective Laser Melting Additive-Manufactured Active Shape-Memory Alloy Honeycomb Arrays. *Actuators* **2022**, *11*, 242. <https://doi.org/10.3390/act11090242>

Academic Editor: Wei Min Huang

Received: 22 July 2022

Accepted: 21 August 2022

Published: 24 August 2022

**Publisher's Note:** MDPI stays neutral with regard to jurisdictional claims in published maps and institutional affiliations.



**Copyright:** © 2022 by the authors. Licensee MDPI, Basel, Switzerland. This article is an open access article distributed under the terms and conditions of the Creative Commons Attribution (CC BY) license (<https://creativecommons.org/licenses/by/4.0/>).

## 1. Introduction

Honeycomb arrays that can deform easily in the in-plane while being stiff enough to withstand the out-of-plane aerodynamic loads have drawn worldwide attention for smart morphing wings [1–5]. Generally, the proposed honeycomb arrays are mostly passive structures [6,7]. The deformation of passive honeycomb arrays is most commonly realized with tightly integrated extra actuators [8–11]. The pressure-based active honeycombs that rely on pressurization within the cells to change the shape are lightweight [12]. However, this will increase the complexity of the smart morphing wings. Hence, active honeycomb arrays that depend on self-deformation rather than extra actuators have gained significant attention for smart morphing wings.

In recent years, shape-memory alloys (SMAs) have been an attractive candidate for manufacturing active honeycomb arrays. Specifically, nickel–titanium (NiTi) SMAs can be used due to their excellent ability to recover the original shape when subjected to suitable characteristic temperatures [13,14]. Okabe et al. [15] described that NiTi SMA honeycomb arrays constructed by conventional sheet-forming processes can present active deformation response. However, conventional manufacturing methods, such as casting, melting and machining, result in increasing the impurity and affecting the functional characteristics of NiTi materials [16]. In addition, conventional processing does not allow for homogeneous control of porosity and geometric flexibility, while complex honeycomb arrays are required by smart morphing wings to achieve better aerodynamic performance. Recently, selective laser melting (SLM) additive manufacturing has been a potential route to produce complex NiTi SMA honeycomb arrays [17–20]. Previous studies have shown

that the SLM-fabricated SMA honeycomb arrays can exhibit excellent active deformation response. Xiong et al. [21] found that SLM-fabricated SMA honeycomb arrays exhibited a shape recovery rate of 99% under compressive deformation when heated above characteristic temperatures. Lu et al. [22,23] described SLM-fabricated SMA honeycomb arrays that presented a shape recovery rate of 100% under folding deformation. However, the actuation performance of the SLM-fabricated active SMA honeycomb arrays has not yet been well-investigated, which is important since the active SMA honeycomb arrays must provide sufficient actuation stress to overcome external resistance and thus realize active deformation.

The authors previously studied the fabrication of NiTi SMA honeycomb unit cells using SLM additive manufacturing for smart morphing wings [24]. In this work, the active SMA honeycomb arrays were analyzed and fabricated by SLM additive manufacturing, and their actuation performance was investigated. This article is organized as follows: Section 2 describes the influence of geometric parameters on actuation performance; Section 3 introduces the manufacturing details of active SMA honeycomb arrays based on SLM additive manufacturing; Section 4 illustrates the actuation performance of SLM-fabricated active SMA honeycomb arrays through experiments. Conclusions are given in Section 5.

## 2. Design of Active SMA Honeycomb Arrays

Over the last few decades, honeycomb arrays with different configurations have been developed and evaluated for smart morphing wings. From most of the previous studies, it is worth noticing that the stress concentration that occurs on the honeycomb arrays often leads to the failure of the arrays during deformation. Therefore, in this section, an arc honeycomb array is introduced, which consists in arc transition to effectively alleviate stress concentration [25]. Further, the influence of geometric parameters on the actuation performance of the active SMA honeycomb array was analyzed through theoretical and finite element analysis (FEA).

### 2.1. Geometry of Active SMA Honeycomb Arrays

In this work, the active SMA honeycomb array used for SLM additive manufacturing is composed of periodic unit cells, as shown in Figure 1a. The unit cell is described by arcs and plates and possesses vertical and horizontal symmetry. Figure 1b shows the geometric parameters of the unit cell. The wall thickness and radius of the arc are represented by the parameters  $t$  and  $R$ . The distance between two arcs is represented by the parameter  $L$ . The width of the plate is represented by  $w$ . The parameter  $X_e = 4R + 2L$  represents the length of the plate. The parameter  $Y_e = 4R + w$  represents the distance between two plates. The parameter  $h$  denotes the thickness of the whole unit cell.

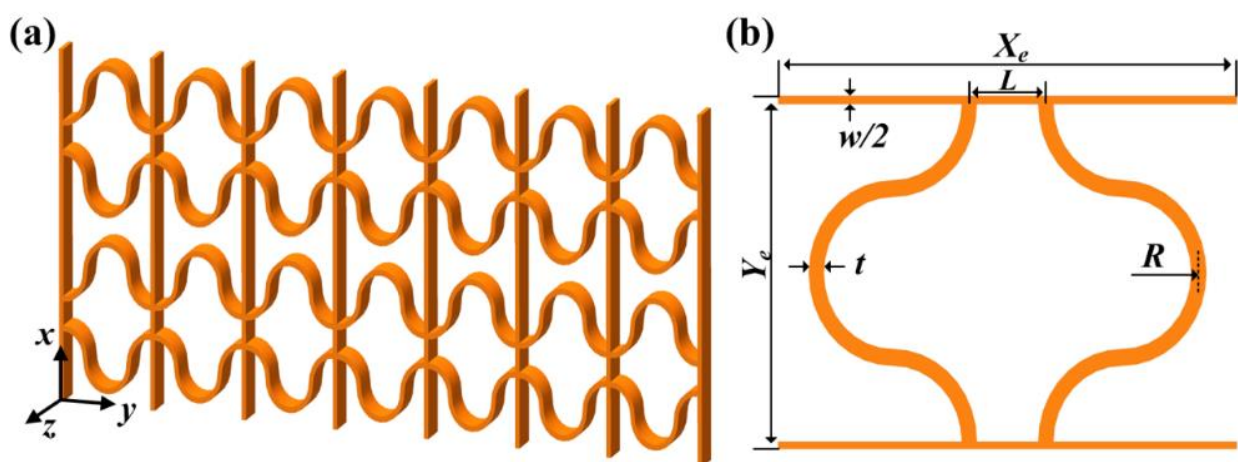


Figure 1. (a) A 3D model of active SMA honeycomb array; (b) geometric parameters.

## 2.2. Analysis of Active SMA Honeycomb Arrays

As described by Sung-min et al. [26], the SMA materials can be considered to have only two states: martensite and austenite. Under this assumption, the actuation stress of an active SMA honeycomb array is linearly related to the in-plane equivalent elastic modulus, which will be affected by geometric parameters. Hence, this section will focus on the influences of geometric parameters on in-plane equivalent elastic modulus.

The in-plane equivalent elastic modulus of the active SMA honeycomb array can be derived from the stress and strain generated by loads applied on the honeycomb array. Considering the symmetry of the array, a quarter unit cell is analyzed instead of the whole unit cell. The quarter unit cell consists of two components: one is the plate, which has almost no effect on the in-plane equivalent elastic modulus; the other is the semi-arc, which plays a principal role as the main elastic component when the honeycomb array is loaded in  $y$  direction. Thus, the semi-arc is mainly analyzed in the derivation of the in-plane equivalent elastic modulus in  $y$  direction. According to the virtual work principle and superposition theory, the non-dimensional in-plane equivalent elastic modulus in  $y$  direction is as follows.

$$\frac{E_y}{E} = \frac{t^3(4R + \omega)}{6\pi R^3(4R + 2L)}, \quad (1)$$

where  $E_y$  is the in-plane equivalent elastic modulus of the active SMA honeycomb array, and  $E$  is the elastic modulus of the raw SMA materials.

In order to validate the theoretical analysis of the in-plane equivalent elastic modulus, the commercial finite element software COMSOL Multiphysics<sup>®</sup> was used to perform the FEA of the active SMA honeycomb arrays. The 3D parametric model of the active SMA honeycomb array was created using the solid mechanics interface. The full size of the active SMA honeycomb array was given as  $2 \times 7$  unit cells. The radius of the arc  $R$  was set as a constant value of 2.5 mm. The  $L/R$  ratio was set as 1, 2, and 3, respectively, while the  $R/t$  ratio was changed from 3 to 7.5 with an increment of 0.5. The values of  $w$  and  $t$  were equal. The material properties, such as the elastic modulus and the Poisson's ratio, were set as 28 GPa and 0.33. For the in-plane tension along  $y$  direction, the boundary conditions of the honeycomb array model were applied with displacement conditions  $u_1 = \delta_y$  along the loading direction on one end, and the opposite end was fully constrained. Free boundary conditions were applied on other surfaces. The finite element meshes in the SMA honeycomb array model are also presented in Figure 2. A minimum element size of  $t/4$  was used during the simulations to ensure convergence of calculation in the analysis, as reported by Liu et al. [25]. The free triangle mesh was built in the  $x$ - $y$  plane and swept along  $z$  direction. The minimum quality and average quality of the element mesh were 0.657 and 0.9056, respectively.

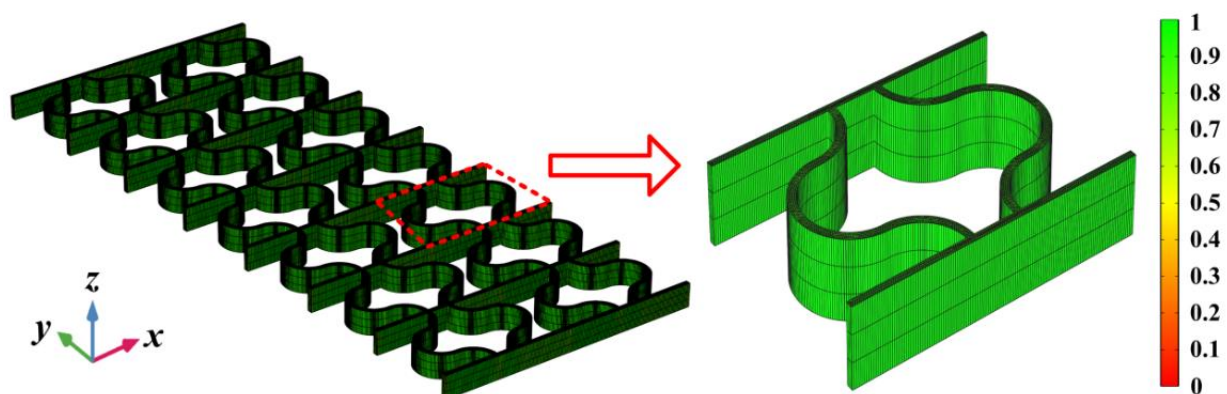
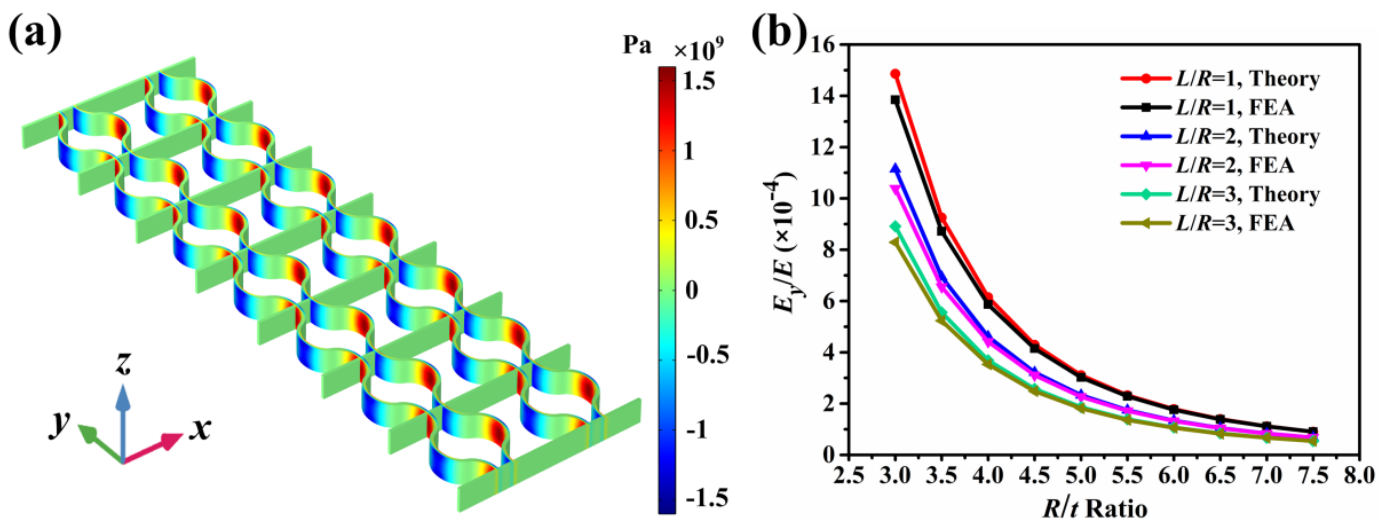


Figure 2. Finite element meshes of the active SMA honeycomb array.

In the calculations, the reaction forces were obtained by aggregating the stresses on the nodes of the respective boundary surfaces, which were employed to calculate the

equivalent stress. Then, the in-plane equivalent elastic modulus was therefore derived from the equivalent stress and the strain applied on the honeycomb array model. Finally, the non-dimensional equivalent elastic modulus was calculated as the ratio between the equivalent elastic modulus and the elastic modulus of raw material.

Figure 3 shows the comparison of the non-dimensional equivalent elastic modulus of the active SMA honeycomb arrays generated from the FEA and theoretical analysis. Figure 3a shows the stress distribution of active SMA honeycomb array corresponding to a tensile strain of 35%. It can be noticed that the SMA honeycomb array undergoes a significant deformation, with the arcs aligned towards the loading direction, and presents uneven local stress distribution. The equivalent stress can be obtained by aggregating the stresses on the nodes of the respective boundary surfaces, and the equivalent elastic modulus can be calculated by the stress-strain relationship of a linear elastic model. Figure 3b shows the variation of non-dimensional in-plane equivalent elastic modulus versus the  $R/t$  ratio at different  $L/R$  ratios. The  $R/t$  ratio was set from 3 to 7.5, while the  $L/R$  ratio was set from 1 to 3. It can be seen that the in-plane equivalent elastic modulus of the active SMA honeycomb arrays can be up to several orders of magnitude lower than that of the raw material. The increase in  $R/t$  ratio and  $L/R$  ratio leads to a significant decrease in non-dimensional in-plane equivalent elastic modulus, which shows a relatively smaller discrepancy between the theoretical and FEA results. When the  $R/t$  ratio and  $L/R$  ratio are 3 and 1, the largest discrepancy can be observed. The in-plane equivalent elastic modulus of theoretical analysis was only 5.6% larger than that of FEA. This phenomenon can be attributed to the fact that theoretical analysis does not take into account the shear deformation of the arcs of the active SMA honeycomb arrays. As one can observe, there is a significant agreement between the theoretical and FEA predictions. The results indicate that the actuation stress can be effectively regulated by adjusting the geometric parameters, which will contribute to the design of active SMA honeycomb arrays for smart morphing wings.



**Figure 3.** (a) Stress distribution of the active SMA honeycomb array at 35% tensile strain; (b) the variation of non-dimensional in-plane equivalent elastic modulus versus the  $R/t$  ratio at different  $L/R$  ratios.

### 3. Fabrication of Active SMA Honeycomb Arrays Based on SLM Process

In this section, SLM additive manufacturing is used to fabricate active SMA honeycomb arrays. The raw materials and SLM process are two key points to fabricate active SMA honeycomb arrays with structural integrity and high quality, which are given as follows.

### 3.1. Raw Materials for SLM Process

In this study, Ni<sub>50.7</sub>Ti<sub>49.3</sub> (at. %) powders produced by Minatech Co., Ltd. (Shenzhen, China) were used for SLM additive manufacturing. A scanning electron microscope (SU8010, Hitachi, Tokyo, Japan) was used to characterize the morphology of the powders. The particle size was measured by a laser diffraction particle size analyzer (Mastersizer3000, Malvern Panalytical, Egham, UK), and the phase components of the powders were examined by X-ray diffraction (XRD) (D8 advance, Bruker Co., Karlsruhe, Germany) with Cu K $\alpha$  radiation. The testing results suggested that the selected Ni<sub>50.7</sub>Ti<sub>49.3</sub> (at. %) powders were spherical and smooth on the surface, as shown in Figure 4a. The particle size distribution of the powders ranged from 14.5–66  $\mu$ m, and the phase components of the powders were mainly comprised of austenite (B2) phases at 18  $^{\circ}$ C, as shown in Figure 4b,c. This indicated that the selected NiTi powders were shown to be of higher bed density, good flowability, and high purity, which are important factors to guarantee the high quality of the SLM-fabricated active SMA honeycomb arrays.

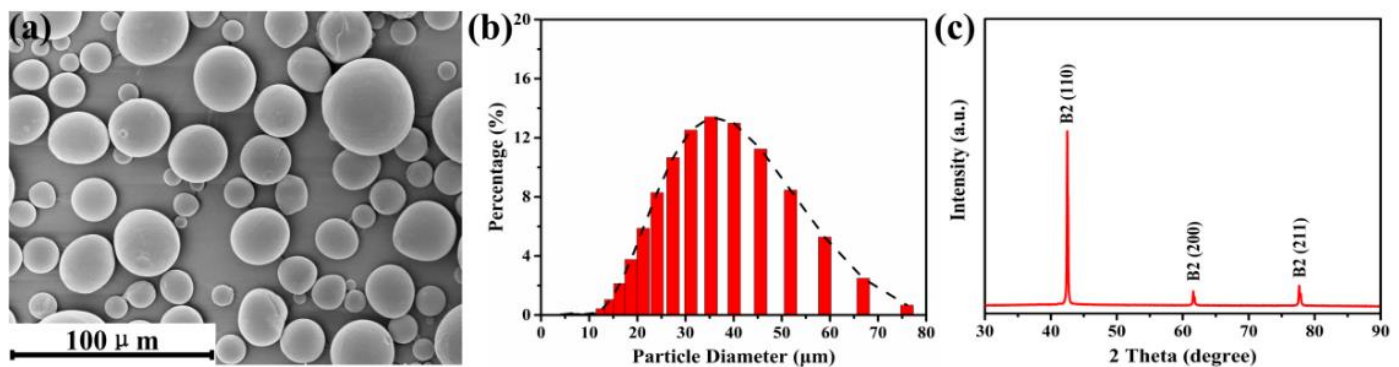


**Figure 4.** The as-received NiTi powders: (a) Powder morphology; (b) particle size distribution [24]; (c) XRD patterns.

### 3.2. SLM Process of Active SMA Honeycomb Arrays

The SLM-150 equipment, which is equipped with a YLR-500-WC ytterbium fiber laser with a maximum power of 500 W, was employed for the SLM process. The SLM process of manufacturing the active SMA honeycomb array is illustrated in Figure 5. The machine used the scraper to create the NiTi powder layer on the NiTi substrate. Then, the NiTi powder layer was fully melted upon the laser selectively scanning with optimal parameters according to the geometry requirements of the active SMA honeycomb array. After solidification, the platform was dropped one layer, and a new NiTi powder layer was laid again. By repeating this process, the whole active SMA honeycomb array was built up layer by layer. The final step was to remove the loose NiTi powder and NiTi substrate. It should be noted that the NiTi substrate is helpful for fabricating active SMA honeycomb arrays with structural integrity.

To produce high-quality active SMA honeycomb arrays, the optimized laser power, scan speed, layer thickness, and hatch spacing were 250 W, 1200  $\text{mm}\cdot\text{s}^{-1}$ , 50  $\mu$ m, and 50  $\mu$ m, respectively. In order to avoid oxidation, the purging cycle was activated to expel the remaining air by a vacuum pump and the high-purity argon gas circulatory protection system until the O<sub>2</sub> content reduced to less than 20 ppm [27–29]. Furthermore, each layer was scanned using a simple linear raster scan strategy through the rotation of 90 $^{\circ}$  [30].

In this study, 3D models of active SMA honeycomb arrays with different parameters were built. The active SMA honeycomb arrays were made of 2  $\times$  7 unit cells with different  $R/t$  ratios. Table 1 shows the dimensions of the identical unit cell with different  $R/t$  ratios. The selected parameters were set as follows:  $R = 2.5$  mm,  $L = 2.5$  mm,  $h = 3$  mm. The values of  $w$  and  $t$  were equal. The wall thicknesses  $t$  were 0.63 mm, 0.5 mm, and 0.42 mm, which were named as S-C4, S-C5, and S-C6, respectively. To investigate the in-plane mechanical properties and actuation stress of the SLM-fabricated active SMA

honeycomb arrays under different tensile pre-strains  $\Delta\varepsilon$ , the width of the plates at both ends of the honeycomb arrays was set as 10 mm for mechanical loading experiments. The active SMA honeycomb arrays with different  $R/t$  ratios were successfully manufactured by SLM additive manufacturing, as shown in Figure 6. The weights of the S-C4, S-C5, and S-C6 honeycomb arrays were 15.9 g, 14.7 g, and 14.0 g, respectively. In addition, the SMA wires with a dimension of  $3 \times 3 \times 80 \text{ mm}^3$  were designed to evaluate the elastic modulus at  $18^\circ\text{C}$ . After SLM processing, the SLM-fabricated SMA wires and honeycomb arrays were subjected to an aging heat treatment of 1 h at  $450^\circ\text{C}$  and were then cooled in the air.

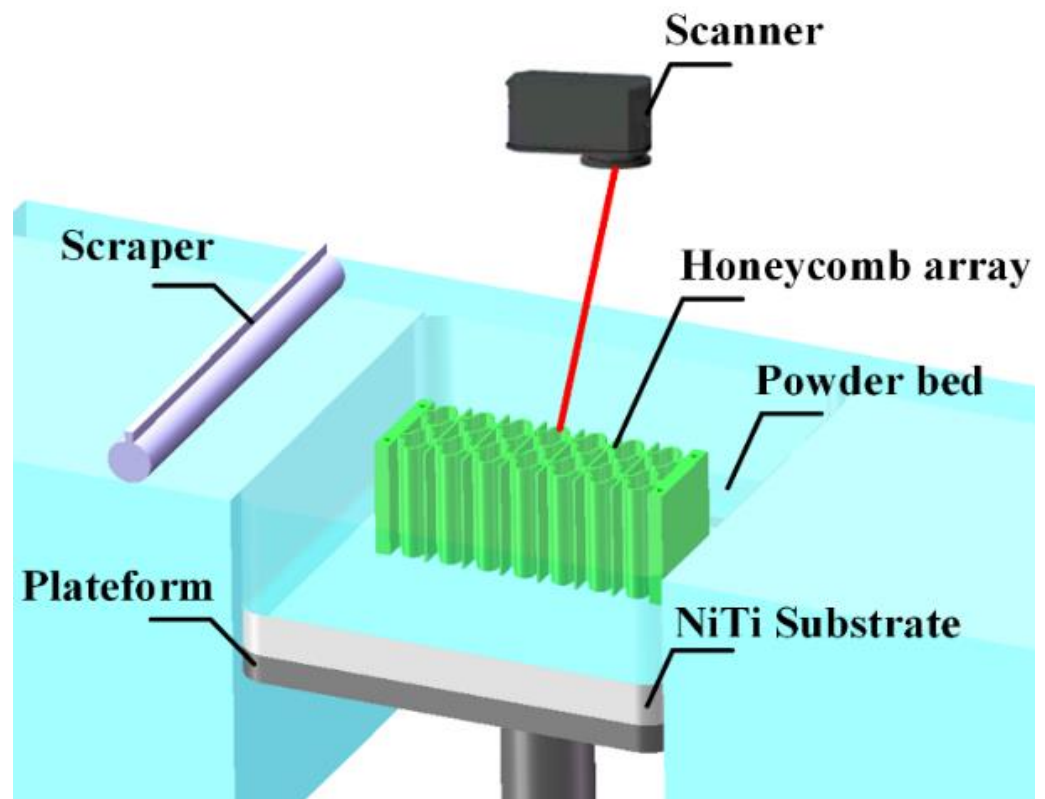


Figure 5. SLM process of manufacturing active SMA honeycomb arrays.

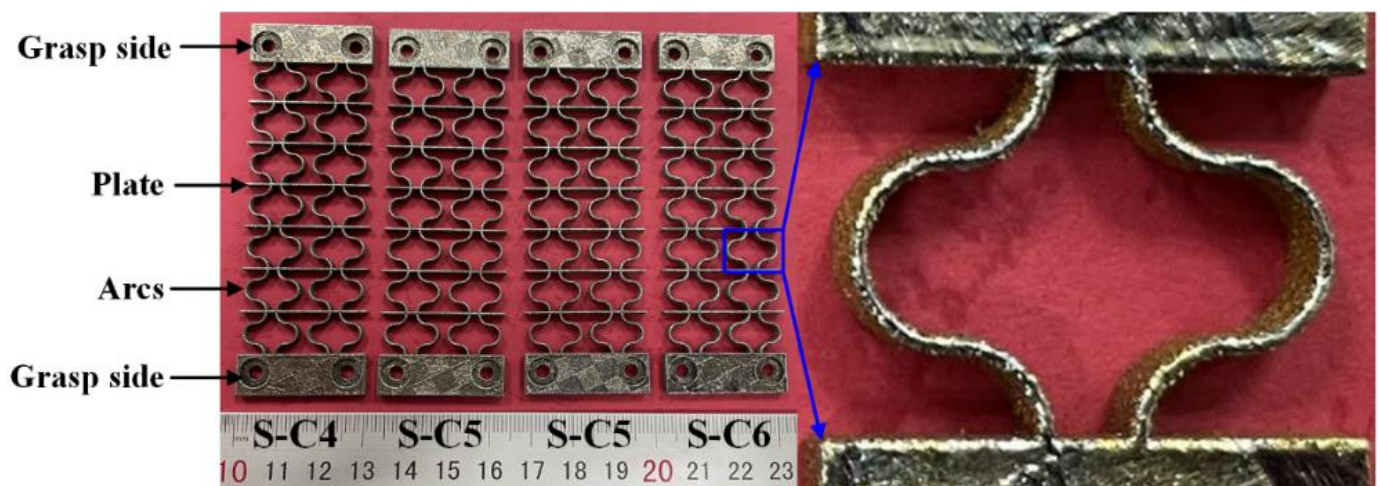


Figure 6. SLM-fabricated active SMA honeycomb arrays.

**Table 1.** The dimensions of the identical unit cells.

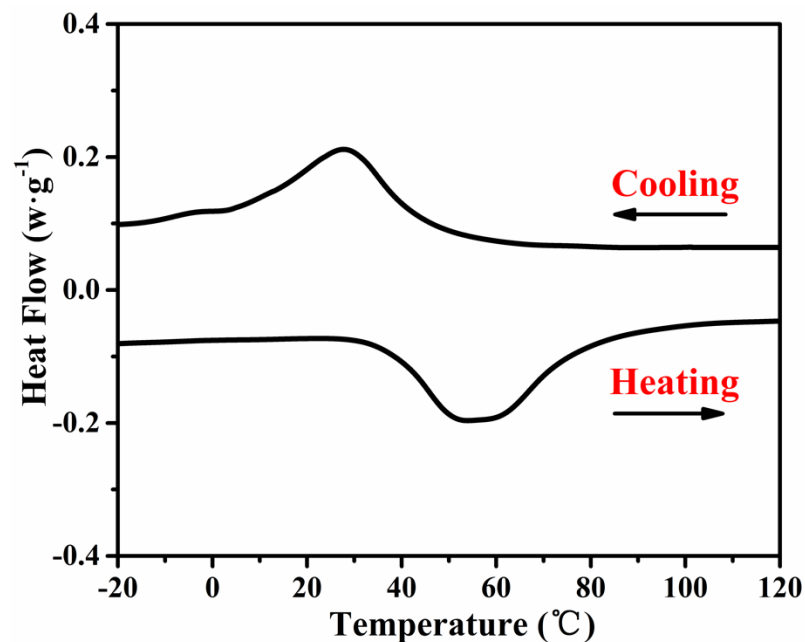
Sample	$t$ (mm)	$R$ (mm)	$L$ (mm)	$w$ (mm)	$h$ (mm)	$R/t$ Ratio
S-C4	0.63	2.5	2.5	0.63	3	4
S-C5	0.50	2.5	2.5	0.50	3	5
S-C6	0.42	2.5	2.5	0.42	3	6

#### 4. Actuation Performance of SLM-Fabricated Active SMA Honeycomb Arrays

In this section, the transformation temperatures of the SLM-fabricated active SMA honeycomb arrays were studied to determine the temperatures at which the active SMA honeycomb arrays exhibit actuation performance. Then, the in-plane mechanical properties of the SLM-fabricated active SMA honeycomb arrays were evaluated. Finally, the actuation stress of the SLM-fabricated active SMA honeycomb arrays under different tensile pre-strains was investigated.

##### 4.1. Characterization of SLM-Fabricated Active SMA Honeycomb Arrays

Understandably, the SLM-fabricated active SMA honeycomb arrays should be heated above certain temperatures in order to exhibit actuation performance. Hence, the transformation temperatures of the SLM-fabricated active SMA honeycomb arrays were measured by a differential scanning calorimetry (DSC) system (DSC25, TA, New Castle, DE, USA) with a heating and cooling rate of  $10\text{ }^{\circ}\text{C}\cdot\text{min}^{-1}$ . The SLM-fabricated samples were cycled thermally twice between  $-20\text{ }^{\circ}\text{C}$  and  $120\text{ }^{\circ}\text{C}$  to eliminate stress influence on transformation temperatures. The transformation temperatures were determined by DSC test results. The curve of the heating process shows the transformation from martensite to austenite, and the curve of the cooling process represents the transformation from austenite to martensite. From the curve of the heating process, the temperatures of  $A_s$  and  $A_f$  can be defined as the start and finish of the austenite transformation, and the temperatures of  $M_s$  and  $M_f$  can be defined as the start and finish of the martensite transformation from the curve of the cooling process, respectively. Thus, the DSC test results define  $A_s = 36.7\text{ }^{\circ}\text{C}$ ,  $A_f = 82.8\text{ }^{\circ}\text{C}$ ,  $M_s = 47.3\text{ }^{\circ}\text{C}$ , and  $M_f = 18.9\text{ }^{\circ}\text{C}$ , as shown in Figure 7. The DSC test results indicated that the SLM-fabricated active SMA honeycomb arrays should be heated above  $A_f$  ( $82.8\text{ }^{\circ}\text{C}$ ); then, they can exhibit actuation performance.

**Figure 7.** DSC test results of the SLM-fabricated active SMA honeycomb array.

An electronic universal testing machine (UTM2503, SUNS, Shenzhen, China) with a load cell of 2 kN and a position accuracy of 0.01 mm was used to evaluate the in-plane mechanical properties and actuation stress of the SLM-fabricated active SMA honeycomb arrays. The samples were loaded in the displacement control mode with a rate of  $1 \text{ mm}\cdot\text{s}^{-1}$  and unloaded in a force control mode with a rate of  $50 \text{ N}\cdot\text{s}^{-1}$ . The heating of the active SMA honeycomb arrays was conducted by a hot-air gun with the power of 1600 W. The distance between the heating equipment and the active SMA honeycomb arrays was 300 mm. The cooling of the active SMA honeycomb arrays was performed by means of liquid nitrogen flow. A K-type thermocouple attached to the honeycomb array surface was used to measure the temperature variation.

#### 4.2. In-Plane Mechanical Properties of SLM-Fabricated Active SMA Honeycomb Arrays

Figure 8a shows the tensile stress–strain response of the SLM-fabricated SMA wire. The curve illustrated is typical of analogous NiTi alloy components tested at  $18^\circ\text{C}$ . During the initial loading stage, the SLM-fabricated SMA wire exhibited linear elastic behavior until the first yield point at 16.8 MPa, after which the stress represented distinctly nonlinear characteristics with the increasing strain loading. When the stress reached 191 MPa, the sample reached the elastic region again. The sample fractured when the stress reached 272 MPa. The result also showed that the elastic modulus  $E_m$  of the SLM-fabricated SMA wire can be estimated as 28 GPa.

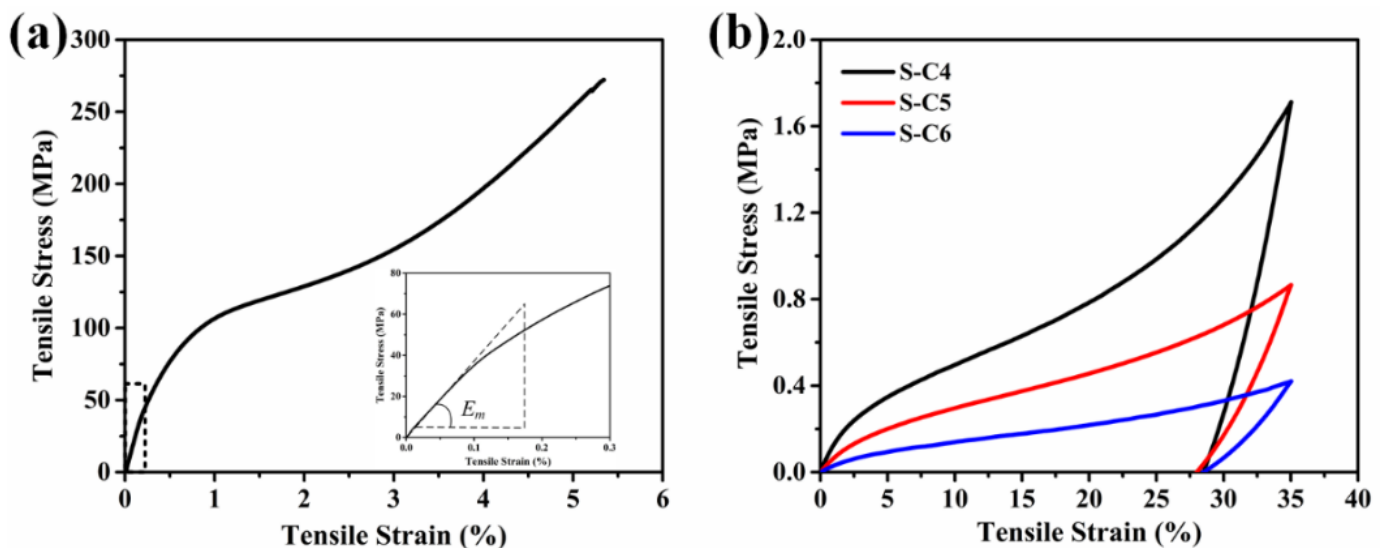


**Figure 8.** Tensile stress–strain responses of the SLM additive-manufactured samples: (a) SMA wire; (b) active SMA honeycomb arrays.

Figure 8b shows the tensile stress–strain responses of the S-C4, S-C5, and S-C6 SLM-fabricated active SMA honeycomb arrays. Compared with SLM-fabricated SMA wires, the SLM-fabricated active SMA honeycomb arrays showed more distinct nonlinear stress–strain responses, which can be attributed to the characteristics of NiTi alloys and honeycomb arrays [31,32]. Moreover, the stress level decreased with the increasing of the  $R/t$  ratio. For instance, the maximum stress of the active SMA honeycomb arrays under tensile strain of 35% decreased from 1.7 MPa to 0.4 MPa when the  $R/t$  ratio increased from 4 to 6. This phenomenon can be attributed to the higher in-plane equivalent elastic modulus of the active SMA honeycomb array with a smaller  $R/t$  ratio, as illustrated in Figure 3b. The results also showed that the in-plane equivalent elastic modulus of the S-C4, S-C5, and S-C6 samples were 16.1 MPa, 7.6 MPa, and 4.1 MPa, respectively. The experimental results are in good agreement with the theoretical and FEA results, as shown in Table 2.

**Table 2.** Comparison of in-plane equivalent elastic modulus of the SLM-fabricated active SMA honeycomb arrays among theoretical, FEA, and experimental results.

Sample	Theoretical (MPa)	FEA (MPa)	Experimental (MPa)
S-C4	17.2	16.4	16.1
S-C5	8.7	8.5	7.6
S-C6	5.0	4.9	4.1

#### 4.3. Actuation Stress of SLM-Fabricated Active SMA Honeycomb Arrays

To evaluate the actuation stress of the SLM-fabricated active SMA honeycomb arrays, the arrays under different tensile pre-strains varying from 10% to 35% were investigated by uniaxial tensile tests. Figure 9 depicts the actuation stress of S-C4, S-C5, and S-C6 SLM-fabricated active SMA honeycomb arrays with different tensile pre-strains. To comprehend these figures clearly, the testing procedure has been sequenced. First, the active SMA honeycomb arrays were loaded by uniaxial tensile tests to the selected tensile pre-strain level and then kept. Next, the active SMA honeycomb arrays were heated up to a temperature above  $A_f$  by a hot-air gun to observe the actuation stress. Lastly, the active SMA honeycomb arrays were cooled down to a temperature below  $M_f$  through an interior fan that could improve the air convection more effectively. The appropriate heating and cooling temperatures of SLM-fabricated SMA honeycomb arrays were 120 °C and 18 °C, which were determined by the first cycle. Different tensile pre-strains of 10%, 15%, 20%, 25%, 30%, and 35% were used for S-C4, S-C5, and S-C6 active SMA honeycomb arrays to observe the actuation stress, respectively. The active SMA honeycomb arrays can achieve stable actuation stresses with a response time of about 50 s.

Figure 9a–c show the actuation stress of the S-C4, S-C5, and S-C6 SLM additive-manufactured active SMA honeycomb arrays under different tensile pre-strains at various temperatures. It can be seen that there are two types of actuation stress curves. The curves in the bottom part represent the heating stage, and those in the top part show the cooling stage. At the same temperature, the actuation stress in the heating stage was significantly lower than that in the cooling stage. The actuation stresses during heating and cooling were not coincident with each other and presented obviously hysteretic behavior, which can be attributed to the hysteresis of SMA materials [33]. The actuation stress increased slowly with the increase in temperature in the initial stage of heating, and increased rapidly and reached stability when the heating temperature changed from 60 °C to 120 °C. In the cooling stage, the actuation stress decreased rapidly and reached stability when the temperature decreased from 120 °C to 18 °C. This phenomenon can be attributed to the reverse transformation from martensite to austenite [34]. When the ambient temperature was 18 °C, the active SMA honeycomb arrays were in martensite phase, and their undeformed crystal structure was twinned (less symmetric). As the tensile pre-strain was applied to the active SMA honeycomb arrays, the crystal structure of martensite changed from twinned to detwinned in the direction of applied deformation (changed orientation of crystal twins), and thus, plastic deformation appeared. When heating the active SMA honeycomb arrays above  $A_f$ , the detwinned martensite transformed into austenite, and the plastic deformation recovered, which caused a two-to-fourfold increase in elastic modulus [35]. As a result, the active SMA honeycomb arrays were able to generate actuation stress during the heating stage when the plastic deformation was constrained. As the temperature decreased, the actuation stress decreased because the austenite transformed into martensite. Furthermore, it was confirmed that the SLM-fabricated active SMA honeycomb arrays can generate sufficient actuation stress along with different tensile pre-strains.

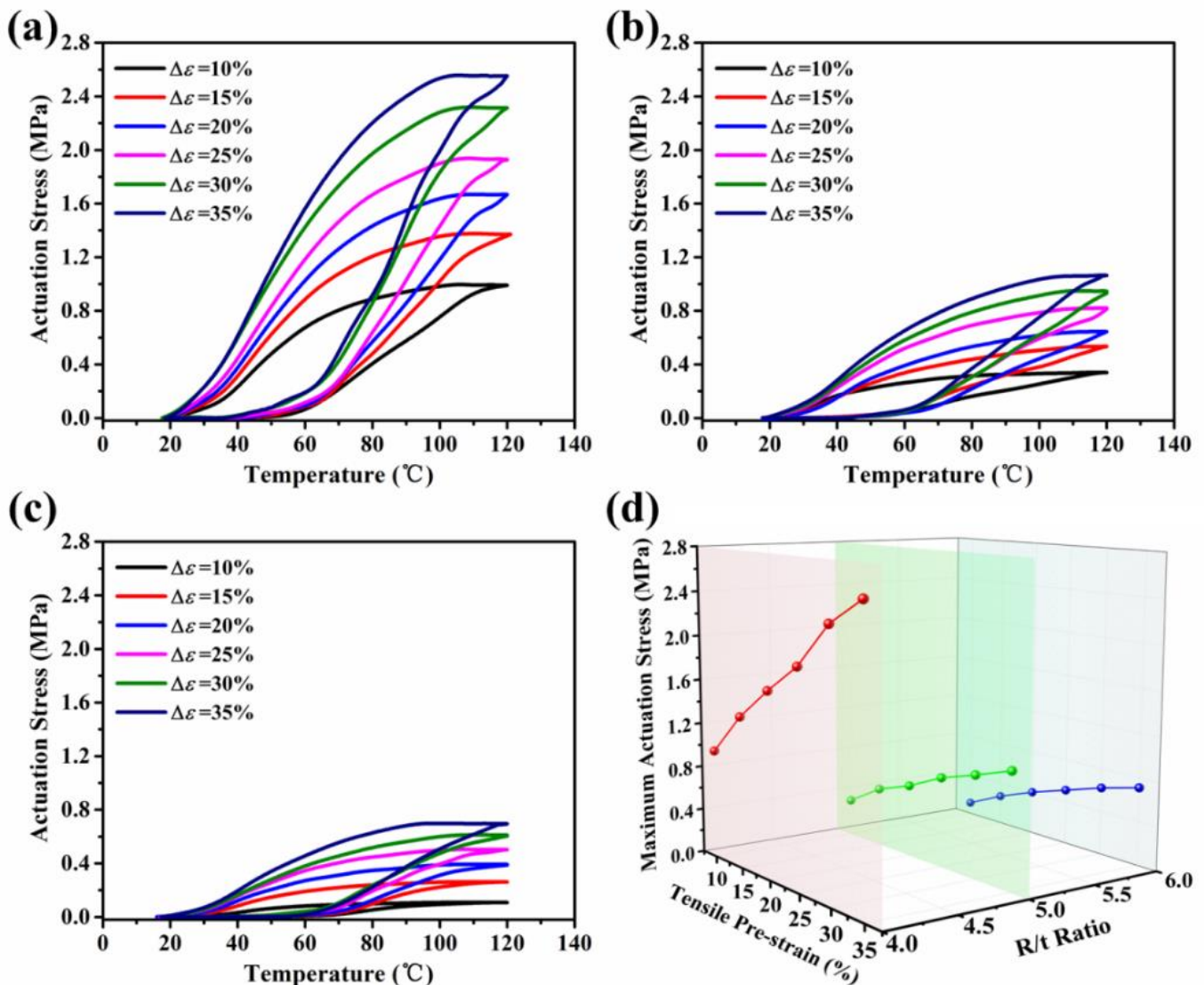


**Figure 9.** Actuation stress of SLM-fabricated active SMA honeycomb arrays: (a) S-C4; (b) S-C5; (c) S-C6; (d) maximum actuation stress.

Figure 9a–c also show that the actuation stress of the SLM-fabricated active SMA honeycomb arrays was highly affected by  $R/t$  ratio and tensile pre-strain. To illustrate this phenomenon clearly, Figure 9d describes the evolution of the maximum actuation stress of the active SMA honeycomb arrays with different  $R/t$  ratios and tensile pre-strains by extracting the data in Figure 9a–c. Despite the fact that the active SMA honeycomb arrays possess obviously hysteretic behavior, the maximum actuation stress almost increased linearly with the increasing of tensile pre-strain, as shown in Figure 9d. For instance, the maximum actuation stresses of S-C4, S-C5, and S-C6 were 0.98 MPa, 0.33 MPa, and 0.11 MPa when the tensile pre-strain was 10%. As the tensile pre-strain increased to 35%, the maximum actuation stresses increased to 2.53 MPa, 1.04 MPa, and 0.71 MPa, respectively. This phenomenon can be illustrated by Hook's law. The SMA can be considered to have two terminal states: martensite and austenite [36]. Under this assumption, the actuation stress of SMA in full austenite phase can be described by a linear relation with the strain [37,38]. Figure 9d also shows that the maximum actuation stress obviously decreases with the increasing of the  $R/t$  ratio and shows a similar change tendency with the in-plane equivalent elastic modulus predictions. This phenomenon can be attributed to the decrease in in-plane equivalent elastic modulus, which can also be described by a linear relation with the actuation stress. The results demonstrate that

the maximum actuation stress of the SLM-fabricated active SMA honeycomb arrays can be designed through varying the geometric parameters and tensile pre-strain. In our previous study, it was demonstrated that the SLM-fabricated active SMA honeycomb arrays can exhibit in-plane tensile deformability capacity above 60%, indicating that the honeycombs meet the requirements of large in-plane deformation of about 50~100% for smart morphing wings [24]. This research shows that the SLM-fabricated active SMA honeycomb arrays can represent excellent actuation force. In particular, the S-C4, S-C5, and S-C6 honeycomb arrays can exhibit higher actuation forces of 288 N, 94 N, and 64 N when the pre-stretched displacement is about 26 mm. This research will contribute to the design of active SMA honeycomb arrays based on SLM additive manufacturing, promoting the engineering applications for smart morphing wings.

## 5. Conclusions

In this work, active SMA honeycomb arrays were fabricated by SLM additive manufacturing, and their actuation performance was investigated. The following conclusions can be drawn: (1) The theoretical and FEA results show that the in-plane equivalent elastic modulus of the active SMA honeycomb arrays decreases with the increase in  $R/t$  ratio and  $L/R$  ratio. In addition, the theoretical analysis results are in good agreement with FEA, which were experimentally verified. (2) The SLM-fabricated active SMA honeycomb arrays show obvious actuation performance and exhibit a higher maximum actuation stress of 2.53 MPa at a  $R/t$  ratio of 4 and a tensile pre-strain of 35%.

In order to realize the application of the SLM-fabricated active SMA honeycomb arrays in smart morphing wings, there is still a lot of work to be done. The weight of the SLM-fabricated SMA honeycombs will be a major consideration as the structure is optimized. The selection of heating equipment will also be considered, satisfying the power application and response time.

**Author Contributions:** Methodology, Investigation, Data curation, Writing—original draft, Writing—review and editing, Y.X.; Funding acquisition, Resources, Data curation, L.Q.; Funding acquisition, Resources, Writing—review and editing, Supervision, S.Y. All authors have read and agreed to the published version of the manuscript.

**Funding:** This research was funded by the National Natural Science Foundation of China (Grant No. 51921003, 51975292) and the Outstanding Youth Foundation of Jiangsu Province of China (Grant No. BK20211519). This work was also supported by the Research Fund of State Key Laboratory of Mechanics and Control of Mechanical Structures (Grant No. MCMS-I-0521K01).

**Institutional Review Board Statement:** Not applicable.

**Informed Consent Statement:** Not applicable.

**Data Availability Statement:** The data presented in this study are available on request from the corresponding author.

**Conflicts of Interest:** The authors declare that they have no known competing financial interest or personal relationship that could have appeared to influence the work reported in this paper.

## References

1. McEvoy, M.A.; Correll, N. Materials that couple sensing, actuation, computation, and communication. *Science* **2015**, *347*, 1261689. [[CrossRef](#)] [[PubMed](#)]
2. Zhou, H.Z.; Plummer, A.R.; Cleaver, D. Distributed actuation and control of a tensegrity-based morphing wing. *IEEE/ASME Trans. Mechatron.* **2022**, *27*, 34–45. [[CrossRef](#)]
3. Li, D.C.; Zhao, S.W.; Ronch, A.D.; Xiang, J.W.; Drofelnik, J.; Li, Y.C.; Zhang, L.; Wu, Y.N.; Kintscher, M.; Monner, H.P.; et al. A review of modelling and analysis of morphing wings. *Prog. Aerosp. Sci.* **2018**, *100*, 46–62. [[CrossRef](#)]
4. Huang, J.; Zhang, Q.H.; Scarpa, F.; Liu, Y.J.; Leng, J.S. Bending and benchmark of zero Poisson's ratio cellular structures. *Compos. Struct.* **2016**, *152*, 729–736. [[CrossRef](#)]
5. Wu, C.; Li, Y.K. AlN-induced reinforcement of nano-amorphous B-C-N compound for TiB<sub>2</sub>-B<sub>4</sub>C ceramic composite. *J. Alloys Compd.* **2020**, *831*, 154074. [[CrossRef](#)]

6. Chen, J.J.; Shen, X.; Li, J.F. Zero Poisson's ratio flexible skin for potential two-dimensional wing morphing. *Aerosp. Sci. Technol.* **2015**, *45*, 228–241. [[CrossRef](#)]
7. Ni, D.R.; Gui, X.; Powderly, K.M.; Cava, R.J. Honeycomb-Structure  $Ru_13$ , A New Quantum Material Related to  $\alpha$ - $RuCl_3$ . *Adv. Mater.* **2022**, *34*, 2106831. [[CrossRef](#)]
8. Sun, J.; Du, L.Z.; Scarpa, F.; Liu, Y.J.; Leng, J.S. Morphing wingtip structure based on active inflatable honeycomb and shape memory polymer composite skin: A conceptual work. *Aerosp. Sci. Technol.* **2021**, *111*, 106541. [[CrossRef](#)]
9. Meyer, P.; Luck, S.; Spuhler, T. Transient dynamic system behavior of pressure actuated cellular structures in a morphing wing. *Aerospace* **2021**, *8*, 89. [[CrossRef](#)]
10. Sun, J.; Gao, H.L.; Scarpa, F.; Liu, Y.J.; Leng, J.S. Active inflatable auxetic honeycomb structural concept for morphing wingtips. *Smart Mater. Struct.* **2014**, *23*, 125023. [[CrossRef](#)]
11. Lv, J.; Ren, X.Y.; Song, C.; Zhang, H.W. Two-scale topology optimization of the 3D plant-inspired adaptive cellular structures for morphing applications. *J. Aerosp. Eng.* **2020**, *33*, 04020032. [[CrossRef](#)]
12. Vos, R.; Barrett, R. Mechanics of pressure-adaptive honeycomb and its application to wing morphing. *Smart Mater. Struct.* **2011**, *20*, 094010. [[CrossRef](#)]
13. McCracken, J.M.; Donovan, B.R.; White, T.J. Materials as machines. *Adv. Mater.* **2020**, *32*, 1906564. [[CrossRef](#)] [[PubMed](#)]
14. Gu, D.D.; Ma, C.L.; Dai, D.H.; Yang, J.K.; Lin, J.; Zhang, H.M.; Zhang, H. Additively manufacturing-enabled hierarchical NiTi-based shape memory alloys with high strength and toughness. *Virtual Phys. Prototy.* **2021**, *16*, S19–S38. [[CrossRef](#)]
15. Okabe, Y.; Sugiyama, H.; Inayoshi, T. Lightweight actuator structure with SMA honeycomb core and CFRP skins. *J. Mech. Des.* **2011**, *133*, 011006. [[CrossRef](#)]
16. Dadbakhsh, S.; Vrancken, B.; Kruth, J.P.; Luyten, J.; Humbeeck, J.V. Texture and anisotropy in selective laser melting of NiTi alloy. *Mater. Sci. Eng. A* **2016**, *650*, 225–232. [[CrossRef](#)]
17. Wang, J.; Pan, Z.X.; Wang, Y.F.; Su, L.H.; Cuiuri, D.; Zhao, Y.H.; Li, H.J. Evolution of crystallographic orientation, precipitation, phase transformation and mechanical properties realized by enhancing deposition current for dual-wire arc additive manufactured Ni-rich NiTi alloy. *Addit. Manuf.* **2020**, *34*, 101240. [[CrossRef](#)]
18. Gu, D.D.; Shi, X.Y.; Poprawe, R.; Bourell, D.L.; Setchi, R.; Zhu, J.H. Material-structure-performance integrated laser-metal additive manufacturing. *Science* **2021**, *372*, 1487. [[CrossRef](#)]
19. Ma, C.L.; Gu, D.D.; Dai, D.H.; Yang, J.K.; Zhang, H.; Guo, M.; Wang, R.; Gao, J.; Chen, W.; Song, Y.J. Tailored pore canal characteristics and compressive deformation behavior of bionic porous NiTi shape memory alloy prepared by selective laser melting. *Smart Mater. Struct.* **2020**, *29*, 095001. [[CrossRef](#)]
20. Ma, C.L.; Gu, D.D.; Setchi, R.; Dai, D.H.; Wu, M.P.; Ma, S.; Miao, X.J. A large compressive recoverable strain induced by heterogeneous microstructure in a  $Ni_{50.6}Ti_{49.4}$  shape memory alloy via laser powder bed fusion and subsequent aging treatment. *J. Alloys Compd.* **2022**, *918*, 165620. [[CrossRef](#)]
21. Xiong, Z.W.; Li, Z.H.; Sun, Z.; Hao, S.J.; Yang, Y.; Li, M.; Song, C.H.; Qiu, P.; Cui, L.S. Selective laser melting of NiTi alloy with superior tensile property and shape memory effect. *J. Mater. Sci. Technol.* **2019**, *35*, 2238–2242. [[CrossRef](#)]
22. Lu, H.Z.; Liu, L.H.; Yang, C.; Luo, X.; Song, C.H.; Wang, Z.; Wang, J.; Su, Y.D.; Ding, Y.F.; Zhang, L.C.; et al. Simultaneous enhancement of mechanical and shape memory properties by heat-treatment homogenization of  $Ti_2Ni$  precipitates in TiNi shape memory alloy fabricated by selective laser melting. *J. Mater. Sci. Technol.* **2022**, *101*, 205–216. [[CrossRef](#)]
23. Lu, H.Z.; Ma, H.W.; Cai, W.S.; Luo, X.; Wang, Z.; Song, C.H.; Yin, S.; Yang, C. Stable tensile recovery strain induced by a  $Ni_4Ti_3$  nanoprecipitate in a  $Ni_{50.4}Ti_{49.6}$  shape memory alloy fabricated via selective laser melting. *Acta Mater.* **2021**, *219*, 117261. [[CrossRef](#)]
24. Xu, Y.S.; Qiu, L.; Yuan, S.F.; Wang, Y. Research on shape memory alloy honeycomb structures fabricated by selective laser melting additive manufacturing. *Opt. Laser Technol.* **2022**, *152*, 108160. [[CrossRef](#)]
25. Liu, W.D.; Li, H.L.; Zhang, J.; Li, H.D. Theoretical analysis on the elasticity of a novel accordion cellular honeycomb core with in-plane curved beams. *J. Sandw. Struct. Mater.* **2020**, *22*, 702–727. [[CrossRef](#)]
26. An, S.M.; Ryu, J.; Cho, M.; Cho, K.J. Engineering design framework for a shape memory alloy coil spring actuator using a static two-state model. *Smart Mater. Struct.* **2012**, *21*, 055009. [[CrossRef](#)]
27. Li, S.; Hassanin, H.; Attallah, M.M.; Adkins, N.J.E.; Essa, K. The development of TiNi-based negative Poisson's ratio structure using selective laser melting. *Acta Mater.* **2016**, *105*, 75–83. [[CrossRef](#)]
28. Wang, X.B.; Yu, J.Y.; Liu, J.W.; Chen, L.G.; Yang, Q.; Wei, H.L.; Sun, J.; Wang, Z.C.; Zhang, Z.H.; Zhao, G.Q.; et al. Effect of process parameters on the phase transformation behavior and tensile properties of NiTi shape memory alloys fabricated by selective laser melting. *Addit. Manuf.* **2020**, *36*, 101545. [[CrossRef](#)]
29. Ma, C.L.; Gu, D.D.; Lin, K.J.; Dai, D.H.; Xia, M.J.; Yang, J.K.; Wang, H.R. Selective laser melting additive manufacturing of cancer pagurus's claw inspired bionic structures with high strength and toughness. *Appl. Surf. Sci.* **2019**, *469*, 647–656. [[CrossRef](#)]
30. Zhang, W.Y.; Tong, M.M.; Harrison, N.M. Scanning strategies effect on temperature, residual stress and deformation by multi-laser beam powder bed fusion manufacturing. *Addit. Manuf.* **2020**, *36*, 101507. [[CrossRef](#)]
31. Otsuka, K.; Ren, X. Physical metallurgy of Ti-Ni-based shape memory alloys. *Prog. Mater. Sci.* **2005**, *50*, 511–678. [[CrossRef](#)]
32. Tatlier, M.S.; Ozturk, M.; Baran, T. Linear and non-linear in-plane behaviour of a modified re-entrant core cell. *Eng. Struct.* **2021**, *234*, 111984. [[CrossRef](#)]

33. Savi, M.A.; Pacheco, P.M.C.L.; Garcia, M.S. Nonlinear geometric influence on the mechanical behavior of shape memory alloy helical springs. *Smart Mater. Struct.* **2015**, *24*, 035012. [[CrossRef](#)]
34. Chopra, I. Review of state of art of smart structures and integrated systems. *AIAA J.* **2002**, *40*, 2145–2187. [[CrossRef](#)]
35. Liu, Y.; Xie, Z.L.; Humbeeck, J.V.; Deklaey, L. Effect of texture orientation on the martensite deformation of NiTi shape memory alloy sheet. *Acta Mater.* **1999**, *47*, 645–660. [[CrossRef](#)]
36. Liang, C.; Rogers, C. Design of shape memory alloy actuators. *J. Intell. Mater. Syst. Struct.* **1997**, *8*, 303–313. [[CrossRef](#)]
37. Guo, Z.; Pan, Y.P.; Wee, L.B.; Yu, H.Y. Design and control of a novel compliant differential shape memory alloy actuator. *Sens. Actuators A Phys.* **2015**, *225*, 71–80. [[CrossRef](#)]
38. Liu, X.L.; Liu, H.; Tan, J.D. Actuation Frequency Modeling and Prediction Shape Memory Alloy Actuators. *IEEE/ASME Trans. Mechatron.* **2021**, *26*, 1536–1546. [[CrossRef](#)]